
Predictability-Aware Compression and Decompression Framework for Multichannel Time Series Data

Ziqi Liu¹ Pei Zeng² Yi Ding¹

¹Department of Computer Science, University of Texas at Dallas

²LexisNexis

{ziqi.liu, yi.ding}@utdallas.edu

pei.zeng@lexisnexis.com

Abstract

Real-world multichannel time series prediction faces growing demands for efficiency across edge and cloud environments, making channel compression a timely and essential problem. Motivated by success of Multiple-Input Multiple-Output (MIMO) methods, we propose a predictability-aware compression-decompression framework to reduce runtime, lower communication cost, and maintain prediction accuracy across diverse predictors. The core idea involves using a circular periodicity key matrix with orthogonality to capture underlying time series predictability during compression and to mitigate reconstruction errors during decompression by relaxing oversimplified data assumptions. Theoretical and empirical analyses show that the proposed framework is both time-efficient and scalable under a large number of channels. Extensive experiments on six datasets across various predictors demonstrate that the proposed method achieves superior overall performance by jointly considering prediction accuracy and runtime, while maintaining strong compatibility with diverse predictors.

1 Introduction

Multichannel time series prediction [21, 32, 6, 10, 2, 22] is widely studied across various application domains, including but not limited to manufacturing process monitoring [11], traffic flow analysis [13], energy consumption tracking [29], and environmental sensing [20], where a channel usually stands for a dimension (e.g., latitude in location data) or a modality (e.g., temperature in environmental sensing). These applications typically stream data from edge-device sensors to cloud-based prediction services, posing practical challenges for transmission and computation. As shown in Figure 1, real-world deployments often involve long time series data with dozens or even hundreds of channels, which strain communication bandwidth and computational resources on edge devices. While compressing along the temporal dimension may reduce input size, it can obscure crucial short-term patterns and make downsampling a potentially risky operation for prediction tasks. These situations make channel compression for time series prediction a timely and valuable research direction.

Despite the importance of channel compression, research on multichannel compression for time series prediction remains limited. General-purpose dimension reduction techniques, including Principal Component Analysis (PCA) [9], Multi-Dimensional Scaling (MDS) [27], Isomap [26], t-distributed Stochastic Neighbor Embedding (t-SNE) [15], and Uniform Manifold Approximation and Projection (UMAP) [16], remain commonly applied in time series prediction tasks. For example, DeepGLO [25] employs PCA-based matrix factorization to extract global features, while another paper [8] applies PCA for temporal dimension reduction. Although these methods aim to capture either temporal inter-channel dependencies or perform intra-channel reduction, they are not specifically designed for time series prediction. As a result, they fail to integrate both inter- and intra-channel information in a unified manner, and do not preserve or reveal the underlying predictability of the data after

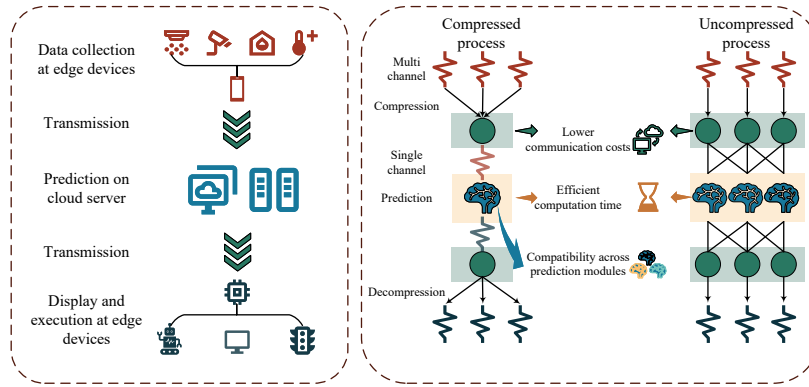


Figure 1: Application requirements in the real world multichannel prediction

compression. Additionally, many of these methods, originally developed for data visualization or non-regression tasks, are unable to accurately reconstruct the original multichannel structure from the predicted compressed representation.

The Multiple-Input Multiple-Output (MIMO) paradigm in signal processing, along with the recent success of MIMONet [17] in image compression, motivates the design of a compression–decompression framework for multichannel time series prediction. During the design process, we identify the following challenges. **First**, preserving the potential predictive information is non-trivial in the compression process. The temporal dependence inherent in time series data stores predictive information and provides a foundation for accurate forecasting. However, such predictability cannot be guaranteed during compression when using current approaches, such as circular convolution with keys sampled from a normal distribution (as in HRR [23]) or a Bernoulli distribution (as in MIMONet). **Second**, oversimplified assumption poses a critical challenge for accurate decompression. Specifically, the assumption of a normal distribution, as adopted in HRR, does not align well with the characteristics of time series data. This mismatch leads to inappropriate decompression module and additional errors, including intra-channel interference across timestamps and inter-channel interference within the same timestamp. **Third**, it is essential to jointly consider the compression-decompression and prediction processes, and explore better overall end-to-end performance. While compressed data naturally leads to reduced computational and transmission time, the compression-decompression steps themselves may introduce additional overhead and information loss, potentially increasing overall time complexity and degrading prediction performance.

To address these challenges, we propose a predictability-aware compression–decompression framework for multichannel time series prediction. In the compression stage, periodicity keys, derived from the least common period across channels via FFT or domain knowledge, are used in a circular convolution process to preserve the predictability information. To mitigate reconstruction errors, the decompression stage employs a circular Toeplitz key matrix and a residual block. To ensure time efficiency, we provide theoretical analysis and introduce sparse encoding and lightweight modules to reduce overhead, particularly under long sequences or edge-device constraints. Extensive experiments on six datasets and multiple backbone predictors (transformer, linear, MLP, and convolutional) demonstrate that our framework consistently improves runtime efficiency and keep prediction accuracy. We also introduce a Cobb–Douglas-based [4] performance index to jointly evaluate accuracy and efficiency, showing that our method achieves superior overall performance and strong compatibility across predictors.

Based on the above descriptions, our main contributions are summarized as follows:

1. A predictability-aware compression–decompression framework is proposed for multichannel time series prediction, which preserves data predictability during compression and minimizes reconstruction error during decompression.
2. Theoretical analyses demonstrate the time efficiency and scalability of the proposed method under a large number of channels, further supported by sparse encoding and lightweight residual components.
3. Extensive experiments demonstrate that the proposed framework achieves lower runtime and superior performance when jointly considering prediction accuracy and computational cost, while maintaining strong compatibility across diverse module architectures.

2 Methodology

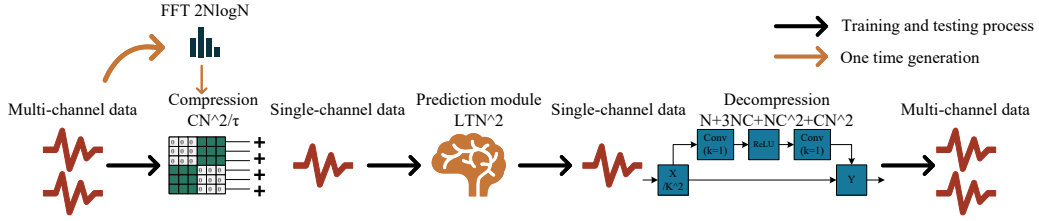


Figure 2: Compression and decompression framework with computational complexity annotations. The predictor (center) is not part of our proposed design and can be replaced by standard single-channel predictors.

As shown in Figure 2, the overall framework consists of three components: a compression module, a decompression module, and a predictor. In the compression module, a multichannel time series input $X_{t-L:t}^C \in \mathbb{R}^{L \times C}$ is transformed into a compressed single-channel representation $X_{t-L:t} \in \mathbb{R}^{L \times 1}$, where L denotes the historical length and C is the number of channels. This single-channel representation is then passed through the predictor to generate the next H time steps, denoted as $X_{t:t+H} \in \mathbb{R}^{H \times 1}$. The predicted sequence is subsequently decompressed to reconstruct the multichannel output $X_{t:t+H}^C \in \mathbb{R}^{H \times C}$.

This work primarily focuses on the compression and decompression modules. Specifically, we investigate how to effectively encode and retain relevant information during compression, and how to reconstruct the multichannel output more accurately by avoiding the oversimplified assumptions that often cause significant reconstruction errors in conventional methods. In the following sections, we sequentially detail the compression process, decompression process, computational complexity analysis, and the overall workflow during training and inference.

2.1 Compression process

The key distinction between the proposed multichannel compression framework and conventional compression methods lies in its predictability-awareness, which refers to the capability to preserve and uncover latent temporal dependencies within time series data. By maintaining these dependencies throughout the compression process, the framework remains compatible with a wide range of predictors, including MLP, linear, convolutional, and transformer-based models that rely on temporal continuity and structure.

In this section, we first define a time series predictability index, followed by the introduction of a predictability-aware compression mechanism, which includes a single-channel encoding strategy and a multichannel combination process.

Time series data predictability

Correlation serves as a central metric for identifying predictive patterns in temporal data. For example, Autoformer [31] replaces the attention mechanism with an auto-correlation module to model temporal dependencies, while Corad [12] leverages Pearson correlation to compress similar segments.

In this work, we define predictability as the degree to which future values depend on historical observations. Following prior research, we adopt the Pearson correlation coefficient to quantify the predictability in time series data. The coefficient, ranging from 0 to 1, measures the strength of the linear association between the former sequence and the current sequence.

Single channel enhancement

Motivated by Holographic Reduced Representations (HRR), a circular convolution process is employed to encode multichannel time series data. To preserve and reveal the potential predictability of each channel, seasonal keys are proposed to guide the compression process. The seasonal key

construction and the channel encoding formulation are presented below:

$$\begin{aligned}
Y_i &= \text{Encode}(K^i, X^i) \\
&= \left[\sum_{z=0}^{n-1} x_z^i k_{(0-z)}, \sum_{z=0}^{n-1} x_z^i k_{(1-z)}, \dots, \sum_{z=0}^{n-1} x_z^i k_{(l-z)} \right] \\
s.t. \quad &k_t = k_{t+\tau}
\end{aligned} \tag{1}$$

Here, $\text{Encode}(\cdot)$ represents the single channel encode process, τ denotes the period of the channel-wise time series, which can be obtained using standard period detection methods such as the Fast Fourier Transform (FFT), or alternatively specified based on domain knowledge.

To demonstrate that the encoding process uncovers the predictability of time series data, a justification is provided based on the Pearson correlation coefficient. The corresponding result is shown below (The detailed derivation is provided in Section A.1.):

$$\begin{aligned}
R &= \frac{\sum_t^{t+\tau} (y_t^i - \bar{y}^1)(y_{t+\tau}^i - \bar{y}^2)}{\sqrt{\sum_t^{t+\tau} (y_t^i - \bar{y}^1)^2} \sqrt{\sum_t^{t+\tau} (y_{t+\tau}^i - \bar{y}^2)^2}} \\
&= \frac{\bar{\gamma}[S_1^2 + \dots + S_\tau^2]}{|\bar{\gamma}|[S_1^2 + \dots + S_\tau^2]} \\
&= 1
\end{aligned} \tag{2}$$

where $\bar{\gamma} > 0$, and S_i is computed in the following formulation,

$$S_t = [y_t^i - y_{\text{mean}}^\tau]^2 \tag{3}$$

Multichannel combination

Following the principle of Least Common Multiple Period (LCMP) in signal processing, if T_1 and T_2 are the fundamental periods of two periodic signals, then their least common multiple $\text{lcm}(T_1, T_2)$ is typically the fundamental period of the combined signal $z(t)$. To maintain inter-channel period consistency and combined representation predictability, all seasonal keys are constructed with the same period $\tau = \text{lcm}(\tau_1, \tau_2, \dots, \tau_C)$. Therefore, for multichannel compression, each channel is first individually encoded using its corresponding periodic key, and the encoded representations are then combined. The overall compression process is shown below:

$$\begin{aligned}
Y &= \sum_{i=1}^C Y^i \\
&= \sum_{i=1}^C \text{Encode}(K, X^i)
\end{aligned} \tag{4}$$

where C is the number of channels.

Compression optimization

Although the complexity of the compression process does not dominate the overall time complexity in the analysis (shown in 2.3), a sparse compression strategy is introduced to further reduce the computational burden on edge devices. Concretely, the sparse compression process is formulated as follows:

$$\begin{aligned}
Y^C &= \sum_{i=0}^C [Y_{0:\tau}^i, Y_{\tau:2\tau}^i, \dots, Y_{(\lfloor \frac{N}{\tau} \rfloor - 1)\tau: \lfloor \frac{N}{\tau} \rfloor \tau}^i] \\
&= \sum_{i=0}^C [\text{Encode}(X_{0:\tau}^i, K), \text{Encode}(X_{\tau:2\tau}^i, K), \dots, \text{Encode}(X_{(\lfloor \frac{N}{\tau} \rfloor - 1)\tau: \lfloor \frac{N}{\tau} \rfloor \tau}^i, K)]
\end{aligned} \tag{5}$$

where $\text{Encode}(\cdot)$ represents single channel encode process, K represents the periodic keys, and i indexes the time series channels. The core idea is to divide each time series into several non-overlapping fragments of length τ , where τ is the least common period (LCP) across all channels.

Any remaining segment that does not complete a full period is omitted during the compression process. The time complexity of the sparse compression operation is:

$$\mathcal{O}(N)_{\text{compression}} = \frac{CN^2}{\tau} \quad (6)$$

When $\tau = \frac{N}{\log N}$, the time complexity reduces to $\mathcal{O}(CN \log N)$.

2.2 Decompression process

The decompression process is designed to mitigate the additional reconstruction errors caused by the oversimplified assumption in HRR, which assumes that the input data follow a normal distribution—an assumption that is often inappropriate for time series data. In this section, we first present the decoding process based on circular correlation, including the analysis of reconstruction errors. We then introduce our proposed method to alleviate these errors.

Decoding process

Motivated by HRR, the decoding process using circular correlation process and periodic keys is defined as follows:

$$\begin{aligned} \tilde{X}^i &= \text{Decode}(K, Y) \\ &= \left[\sum_{z=0}^{n-1} y_z k_{z-0}, \sum_{z=0}^{n-1} y_z k_{z-1}, \dots, \sum_{z=0}^{n-1} y_z k_{z-h} \right] \\ &= \left[\left(\sum k^2 \right) (x_0^0 + x_0^1 + \dots + x_0^{l-1}) + \eta, \left(\sum k^2 \right) (x_1^0 + x_1^1 + \dots + x_1^{C-1}) + \eta \right. \\ &\quad \left. , \dots, \left(\sum k^2 \right) (x_h^0 + x_h^1 + \dots + x_h^{C-1}) + \eta \right] \end{aligned} \quad (7)$$

where η denotes the accumulated intra-channel errors resulting from different timestamps within the same channel. HRR assumes that both the data X and the key K follow a normal distribution, which allows intra-channel interference to be reduced. However, this assumption does not hold for time series data and periodic keys, thereby motivating the design of a new decompression process. In addition to intra-channel errors, recovering the i -th channel result \tilde{X}^i also suffers from inter-channel interference introduced by other channels at the same timestamp, further degrading reconstruction quality.

Intra-channel errors reduction

To reduce the effect of intra-channel errors, we adopt an orthogonal circular matrix for keys K . The characteristic of a circular matrix [5] is that each column is a cyclic shift of the previous column, meaning it is entirely determined by its first row. An orthogonal circular matrix is a special type of circular matrix that satisfies the orthogonality condition $K^T K = I$, where I is the identity matrix. (Obtained from two times FFT [24]).

Based on the properties of the orthogonal circular keys Matrix, different shifts (or permutations) of the key vectors are mutually orthogonal. During the decoding process, when recovering a specific timestamp, the multiplication of the corresponding key vector with those from other timestamps results in zero due to the orthogonality. Consequently, only the current timestamp's contribution remains when decoded using the key matrix (see Appendix A.2 for details). The updated reconstruction based on the orthogonal circular key matrix is given by:

$$\tilde{X}^i = \left(\sum k^2 \right) \cdot \begin{bmatrix} x_0^0 + x_0^1 + \dots + x_0^{C-1} \\ x_1^0 + x_1^1 + \dots + x_1^{C-1} \\ \dots \\ x_{n-1}^0 + x_{n-1}^1 + \dots + x_{n-1}^{C-1} \end{bmatrix}^T \quad (8)$$

Inter-channel errors reduction

To eliminate inter-channel interference and restore channel-wise fidelity, we introduce a residual correction module. The main idea is that utilize the residual process to adaptively remove the other channel's effect on the same timestamps. The process is shown below,

$$\tilde{X} = \text{Dense} \left(\frac{\text{Copy}(\text{Decode}(K, Y))}{\sum k^2} + \text{Residual} \left(\frac{\text{Copy}(\text{Decode}(K, Y))}{\sum k^2} \right) \right) \quad (9)$$

where the $\text{Residual}(\cdot)$ denotes a lightweight residual block consisting of two convolution layers with one ReLU activation, and $\text{Copy}(\cdot)$ denotes either duplicating the decoded result to match the number of channels or using a learnable transformation (e.g., a dense layer) to project it to the desired channel dimension. This correction allows the model to disentangle individual channels from the shared reconstruction, thereby enhancing decompression precision. The associated time complexity is given in Equation 11.

2.3 Time complexity analysis

The time complexity of the proposed framework is derived by considering the complete pipeline, including compression, decompression, and prediction. The total computational complexity is given by:

$$\begin{aligned} \mathcal{O}(N)_{\text{comp}} &= \underbrace{LTN^2}_{\text{Prediction}} + \underbrace{\frac{CN^2}{\tau} + 2N \log N}_{\text{Compression}} + \underbrace{N + 3NC + NC^2 + CN^2}_{\text{Decompression}} \\ &\approx LTN^2 + \frac{CN^2}{\tau} + CN^2, \quad (\text{neglecting lower-order terms}) \end{aligned} \quad (10)$$

where T denotes the number of training epochs, N is the number of timestamps, C ($C < N$) is the number of channels, L is the depth of the predictor, and τ is the least common multiple (LCM) period across different channels. The time complexity of the residual block in the decompression process is given by:

$$\begin{aligned} \mathcal{O}(N)_{\text{decompression}} &= \mathcal{O}(\text{Divide}) + \mathcal{O}(\text{Conv}) + \mathcal{O}(\text{Relu}) + \mathcal{O}(\text{Conv}) + \mathcal{O}(\text{Residual}) + \mathcal{O}(\text{Dense}) \\ &= N + NC + NC + NC^2 + NC + CN^2 \\ &= N + 3NC + NC^2 + CN^2 \end{aligned} \quad (11)$$

In contrast, a naive multichannel predictor without compression incurs the following computational complexity:

$$\mathcal{O}(N)_{\text{naive}} = LTCN^2. \quad (12)$$

To determine the minimum number of channels C for which the proposed method achieves lower computational cost, the two complexities are compared:

$$\begin{aligned} \mathcal{O}(N)_{\text{naive}} &> \mathcal{O}(N)_{\text{comp}} \\ LTCN^2 &> LTN^2 + CN^2 + \frac{CN^2}{\tau} \\ \Rightarrow C &> \frac{LT}{LT - 1 - \frac{1}{\tau}} \quad (\text{assuming } LT \gg 1 \text{ and } \frac{1}{\tau} \rightarrow 0) \end{aligned} \quad (13)$$

Under the assumptions $LT \gg 1$ and $\frac{1}{\tau} \rightarrow 0$, the lower bound reduces to $C > 1$, indicating that the proposed framework offers a computational advantage when the number of channels exceeds one. Furthermore, since the overhead introduced by compression and decompression is subdominant in the asymptotic regime, it does not alter the scaling advantage of the proposed method.

2.4 Training strategy

Normalization

Following Dish-TS [7], a standard normalization is applied after compression and reversed before decompression. Specifically, each compressed segment is normalized by subtracting its mean and dividing by its standard deviation to stabilize outputs across different periods τ . During inference, the predicted outputs are denormalized accordingly to restore the original scale.

Training and testing process

The total training objective is composed of three components:

$$\begin{aligned} \mathcal{L} &= \mathcal{L}_{\text{Prediction}} + \mathcal{L}_{\text{Regulation}} + \mathcal{L}_{\text{Normal}} \\ &= (X_{\text{Label}} - X_{\text{Predict}})^2 + \alpha \left(\sum_1^C |X_{\text{Residual}}| - \sum_1^C X_{\text{Predict}} \right)^2 + \beta (\varphi_Y - \varphi_{\hat{Y}})^2 \end{aligned} \quad (14)$$

Here, $\mathcal{L}_{\text{Prediction}}$ denotes the prediction error, $\mathcal{L}_{\text{Regulation}}$ denotes the regulation term for the decompression process, $\mathcal{L}_{\text{Normal}}$ denotes the mean consistency between the predicted and true signals.

To enhance the numerical stability during the training of the compression–prediction–decompression framework, we adopt a scale-invariant gradient clipping strategy [14]. Specifically, given a parameter w and its corresponding gradient g , we modify the gradient as follows:

$$g \leftarrow g \times \min\left(1, \frac{\alpha \|w\|}{\|g\|}\right), \quad (15)$$

where $\alpha > 0$ is a hyperparameter controlling the clipping threshold. This approach adaptively scales the gradient based on the magnitude of the parameter, ensuring that the update is proportional to the parameter norm. Such scale-invariant clipping prevents exploding gradients without introducing excessive regularization, and is particularly effective in architectures with large scale variations across different layers (see Appendix A.5 for details).

3 Experiments

3.1 Experimental settings

Datasets

To demonstrate the effectiveness of our predictability-aware compression and decompression framework (PCDF) in multichannel time series prediction, we evaluate it on a diverse set of application datasets collected from edge device sensors. These datasets include traffic data (NYC Taxi [19], DC Bike [1]), energy data (solar energy generation [18], electricity consumption [28]), weather data [3], and manufacturing data (gas sensor array drift [30]).

Baselines and setup

We apply our compression–decompression framework to multiple existing predictors (MLP, Transformer, Linear, and Convolution, as detailed in Appendix A.7). Throughout the paper, we refer to each such combination as an integration (e.g., PCDF-MLP, PCDF-Trans, PCDF-Linear, PCDF-Conv). We compare these integrations with state-of-the-art models, including PatchTST [21], Autoformer [31], HDMixer [10], DLinear [32], MSGNet [2], and TSMixer [6], to evaluate changes in performance and runtime trade-offs. All models follow the same experimental setup, with the number of prediction channels set to $C \in \{5, 10, 20, 30, 40\}$. All experiments are conducted on two NVIDIA RTX 4090 GPUs, each equipped with 24 GB of memory.

3.2 Prediction MSE and runtime with Comprehensive analysis

Following the idea of the Cobb–Douglas production function [4], which uses a multiplicative combination to model the joint contribution of multiple factors, we combine MSE and computational time in a similar fashion to capture the trade-off and enable a comprehensive analysis of prediction accuracy and computational efficiency.

Based on the MSE and runtime results for all models (see details in Appendix A.8 and Appendix A.9), the multiplicative combination of MSE and runtime—referred to as the Cobb–Douglas production index—is presented in Table 1 and formally defined in Equation 16. The compression–decompression integrations achieve lower combined index values compared to the representative baseline models across different datasets in most cases. These results suggest that the compression–decompression framework has the potential to achieve better overall performance with reduced prediction time and lower prediction errors.

$$\text{Cobb–Douglas production index} = \text{MSE} \cdot \text{Runtime} \quad (16)$$

From the perspective of different datasets, those with clear periodic patterns, such as Electricity, tend to exhibit lower combined index values. This indicates that such datasets either require less computational time or result in lower prediction errors after processing, leading to better overall performance. Conversely, datasets with less pronounced periodic patterns tend to have higher combined index values, reflecting increased prediction errors or longer computational times.

Table 1: Cobb–Douglas production index (lower values indicate better overall performance)

Dataset & Channel	MLP based comparison			Transformer based comparison			Linear based comparison			
	PCDF-MLP	TSMixer	Ratio (MLP/Ts)	PCDF-Trans	PatchTST	Ratio (Trans/Patch)	PCDF-Linear	HDMixer	Ratio (Linear/HD)	
NYC taxi 0.1/24	5	0.000459	0.000397	1.156	0.000340	0.000716	0.475	0.000310	0.002464	0.126
	10	0.000524	0.000567	0.924	0.000386	0.001026	0.376	0.000348	0.003966	0.088
	20	0.000581	0.000735	0.790	0.000478	0.001853	0.258	0.000968	0.006231	0.155
	30	0.000664	0.000885	0.750	0.000564	0.002532	0.223	0.000528	0.007694	0.069
	40	0.000761	0.000969	0.785	0.000745	0.003158	0.236	0.000632	0.012362	0.051
DC bike 0.3/30	5	0.000539	0.000647	0.833	0.000413	0.001063	0.389	0.000505	0.009265	0.055
	10	0.000619	0.000864	0.716	0.000414	0.001693	0.244	0.000366	0.016486	0.022
	20	0.000691	0.001150	0.601	0.000643	0.003208	0.200	0.000543	0.028265	0.019
	30	0.000804	0.001345	0.598	0.000949	0.003812	0.249	0.000622	0.037110	0.017
	40	0.000984	0.001500	0.656	0.001235	0.005163	0.239	0.003392	0.050074	0.068
Electricity 0.1/24	5	0.000299	0.000215	1.391	0.000219	0.000337	0.650	0.000169	0.001188	0.142
	10	0.000242	0.000285	0.849	0.000234	0.000611	0.383	0.000195	0.001984	0.098
	20	0.000394	0.000448	0.879	0.000319	0.000972	0.328	0.000335	0.004585	0.073
	30	0.000430	0.000523	0.822	0.000404	0.001315	0.307	0.000312	0.007746	0.040
	40	0.000525	0.000697	0.753	0.000534	0.001740	0.307	0.000425	0.013574	0.031
Solar energy 0.25/24	5	0.000765	0.000980	0.781	0.000538	0.001336	0.403	0.000508	0.007004	0.073
	10	0.000586	0.000915	0.641	0.000506	0.001576	0.321	0.000416	0.007520	0.055
	20	0.000631	0.001087	0.581	0.000541	0.002316	0.234	0.000512	0.015104	0.034
	30	0.000730	0.001384	0.527	0.000625	0.003065	0.204	0.000596	0.026226	0.023
	40	0.000857	0.001401	0.612	0.000750	0.003609	0.208	0.000869	0.039396	0.022
Sensor drift 0.1/30	5	0.000548	0.001070	0.512	0.000434	0.001573	0.276	0.000368	0.010083	0.037
	10	0.000638	0.001385	0.461	0.000456	0.002456	0.186	0.000472	0.013823	0.034
	20	0.000846	0.002084	0.406	0.000666	0.004751	0.140	0.000792	0.024024	0.033
	30	0.000951	0.002270	0.419	0.000841	0.006407	0.131	0.000861	0.031081	0.028
	40	0.001077	0.002886	0.373	0.000929	0.009078	0.102	0.000850	0.033141	0.026
Weather 0.1/25	5	0.000342	0.000434	0.788	0.000273	0.000989	0.276	0.000425	0.001812	0.235
	10	0.000394	0.000547	0.720	0.000306	0.001193	0.257	0.000267	0.003822	0.070
	20	0.000569	0.000731	0.778	0.000382	0.002106	0.182	0.000391	0.007379	0.053
	30	0.000590	0.000883	0.668	0.000535	0.003086	0.173	0.000475	0.011419	0.042
	40	0.000630	0.001081	0.583	0.000528	0.004326	0.122	0.000533	0.022849	0.023

3.3 Variance analysis of MSE, runtime, and composite index across datasets

Figure 3 shows the variance of MSE and runtime. The integrations exhibit lower variance across different datasets compared to their corresponding base models, indicating that our framework provides better stability for the underlying predictors.

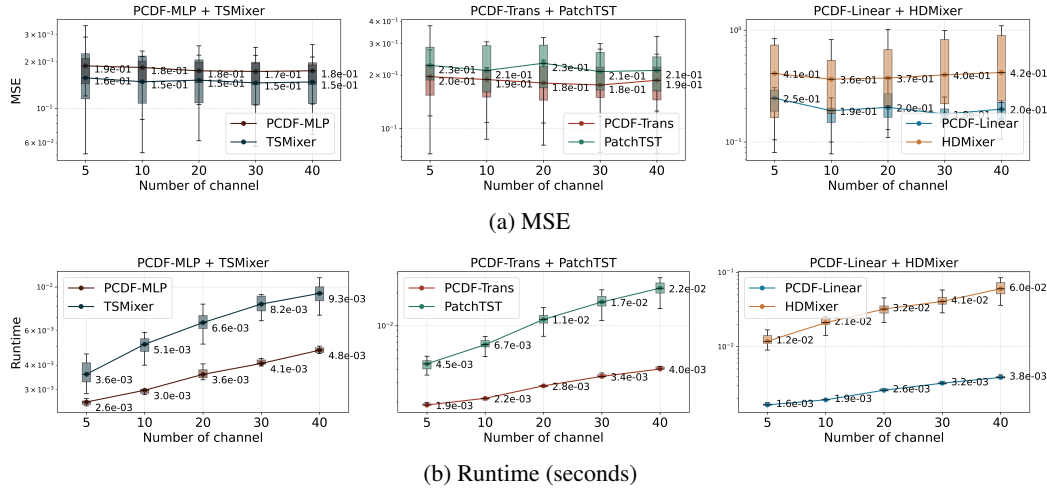


Figure 3: Boxplot of MSE and runtime across channel configurations and datasets

In terms of value distribution, the integrations generally achieve lower values than their base models, except for the PCDF-MLP and its corresponding base model TSMixer in the MSE metric. This suggests that our framework can effectively reduce runtime, decrease MSE, and improve overall performance compared to other methods built upon the same predictors—despite the exception observed with TSMixer.

3.4 Ablation results

In the ablation study, a classic encoder–decoder framework is used to replace the compression and decompression components in order to justify the efficiency of the proposed framework. In addition,

Table 2: Compression-decompression framework ablation study via MSE

Method	NYC taxi	DC bike	Electricity	Solar energy	Sensor drift
Compression-decompression	0.1799515	0.215305	0.10726	0.2172095	0.238878
Randomkey-decompression	0.19826	0.259521	14.803542	18.559643	0.253261
Compression-decoder	0.213246	1257.967764	0.2435455	9.832429	0.5709225
Encoder-decompression	0.323226	5.4924415	143.518735	1.998019	12.7464045
Encoder-decoder	0.1545935	1.5364435	0.173675	1.6343485	0.302809

a random key is used in place of the periodic key to evaluate the effectiveness of the compression component guided by periodic information. Therefore, the ablation study includes four variants: (1) random-key compression–decompression, (2) compression–decoder, (3) encoder–decompression, and (4) encoder–decoder.

In the random-key variant, the results vary significantly across datasets, suggesting that the random key fails to uncover the underlying predictive patterns in some datasets. This highlights the importance of using the periodic key within the compression–decompression framework.

For the compression–decoder and encoder–decompression variants, since compression and decompression are co-designed and interdependent, using only one of the components leads to unstable results. This indicates that optimal performance relies on the synergy between both compression and decompression modules.

In the encoder–decoder variant, although lower MSE is observed on the NYC Taxi dataset, the performance remains unstable overall. This may be attributed to the fact that the encoder cannot effectively preserve or extract predictive patterns, and the corresponding decoder may fail to recover the single-channel signal in a lossless manner. The inferior and unstable results of these ablation variants validate the superiority of our framework in both extracting latent predictive information during compression and performing accurate reconstruction during decompression.

4 Conclusion

This paper proposes a novel predictability-aware compression–decompression framework tailored for multichannel time series prediction. By leveraging a periodicity-guided convolution process with circularly orthogonal key matrices, the framework effectively preserves latent temporal dependencies during compression and mitigates reconstruction errors during decompression. Theoretical analyses verify that the introduced compression–decompression components do not dominate the overall computational complexity, while practical designs such as sparse encoding and lightweight residual modules further alleviate the burden on edge devices. Extensive experiments across diverse datasets and prediction backbones demonstrate that our framework consistently achieves lower runtime and improved prediction accuracy, as evidenced by reduced Cobb–Douglas production indices. Furthermore, ablation results confirm the necessity of jointly optimizing both compression and decompression processes. Overall, this work offers a flexible and efficient solution for compressing multichannel time series data without sacrificing predictive performance, paving the way for more resource-efficient forecasting in edge–cloud environments.

Limitations and future work

Despite strong model compatibility, the framework requires retraining when applied to new domains, limiting its out-of-domain generalization. Additionally, under extreme compression ratios, training instability such as gradient explosion may occur. While this is alleviated via scale-invariant gradient clipping, we attribute the root cause to the large dimensional disparity between compressed and decompressed representations. Future work will explore principled mechanisms to bridge this gap and enhance training robustness.

Broader impacts

The proposed framework significantly reduces computational resources on edge devices and communication requirements on the local network, enabling deployment in bandwidth- or resource-constrained environments. This has practical societal benefits in both developed and underdeveloped areas. For example, in AI smart-city, fast edge predictions improve flow and reduce emissions. Correspondingly, in rural agriculture, lightweight on-device prediction enables timely decision-making despite outdated hardware and poor connectivity.

References

- [1] Capital Bikeshare, Capital Bikeshare Trip History Data. Available at: <https://s3.amazonaws.com/capitalbikeshare-data/index.html>. Accessed: May 3, 2025.
- [2] W. Cai et al., MSGNet: Learning Multi-Scale Inter-series Correlations for Multivariate Time Series Forecasting, AAAI, pp. 11141–11149, 2024.
- [3] J. Cejpek and Meteostat contributors, Meteostat: Historical Weather and Climate Data. Available at: <https://meteostat.net/>. Accessed: May 15, 2025.
- [4] C. W. Cobb et al., A Theory of Production, *The American Economic Review*, vol. 18, no. 1, pp. 139–165, 1928.
- [5] P. J. Davis, *Circulant Matrices*, 2nd ed., Chelsea, New York, 1994.
- [6] V. Ekambaram et al., TSMixer: Lightweight MLP-Mixer Model for Multivariate Time Series Forecasting, KDD, pp. 459–469, 2023.
- [7] W. Fan et al., Dish-TS: A General Paradigm for Alleviating Distribution Shift in Time Series Forecasting, AAAI, pp. 7522–7529, 2023.
- [8] J. Gao et al., Revisiting PCA for Time Series Reduction in Temporal Dimension, arXiv preprint, arXiv:2404.00000, 2024.
- [9] H. Hotelling et al., Analysis of a complex of statistical variables into principal components, *Journal of Educational Psychology*, vol. 24, no. 6, pp. 417–441, 1933.
- [10] Q. Huang et al., HDMixer: Hierarchical Dependency with Extendable Patch for Multivariate Time Series Forecasting, AAAI, pp. 12608–12616, 2024.
- [11] K. Jang et al., Explainable Artificial Intelligence for Fault Diagnosis of Industrial Processes, *IEEE Transactions on Industrial Informatics*, vol. 21, no. 1, pp. 4–11, 2025.
- [12] A. Khelifati et al., Corad: Correlation-aware Compression of Massive Time Series Using Sparse Dictionary Coding, *IEEE Big Data*, pp. 2289–2298, 2019.
- [13] X. Liu et al., LargeST: A Benchmark Dataset for Large-Scale Traffic Forecasting, *NeurIPS*, 2023.
- [14] Z. Li et al., Robust Training of Neural Networks Using Scale Invariant Architectures, *ICML*, pp. 12656–12684, 2022.
- [15] L. van der Maaten et al., Visualizing Data using t-SNE, *Journal of Machine Learning Research*, pp. 2579–2605, 2008.
- [16] L. McInnes et al., UMAP: Uniform Manifold Approximation and Projection for Dimension Reduction, arXiv preprint, arXiv:1802.03426, 2018.
- [17] N. Menet et al., MIMONets: Multiple-Input-Multiple-Output Neural Networks Exploiting Computation in Superposition, *NeurIPS*, 2023.
- [18] National Renewable Energy Laboratory, Solar Power Data for Integration Studies. Available at: <https://www.nrel.gov/grid/solar-power-data.html>. Accessed: May 4, 2025.
- [19] New York City Taxi and Limousine Commission, TLC Trip Record Data. Available at: <https://www.nyc.gov/site/tlc/about/tlc-trip-record-data.page>. Accessed: May 1, 2025.
- [20] T. Nguyen et al., Scaling Transformer Neural Networks for Skillful and Reliable Medium-Range Weather Forecasting, *NeurIPS*, 2024.
- [21] Y. Nie et al., A Time Series is Worth 64 Words: Long-term Forecasting with Transformers, *ICLR*, 2023.

- [22] S. Palaskar et al., AutoMixer for Improved Multivariate Time-Series Forecasting on Business and IT Observability Data, AAAI, pp. 22962–22968, 2024.
- [23] T. A. Plate, Holographic Reduced Representations, IEEE Transactions on Neural Networks, vol. 6, no. 3, pp. 623–641, 1995.
- [24] R. Wang et al., Orthogonal Circulant Structure and Chaotic Phase Modulation based Analog to Information Conversion, Signal Processing, vol. 144, pp. 104–117, 2018.
- [25] R. Sen et al., Think Globally, Act Locally: A Deep Neural Network Approach to High-Dimensional Time Series Forecasting, NeurIPS, vol. 32, 2019.
- [26] J. B. Tenenbaum et al., A Global Geometric Framework for Nonlinear Dimensionality Reduction, Science, vol. 290, pp. 2319–2323, 2000.
- [27] W. S. Torgerson et al., Multidimensional Scaling: I. Theory and Method, Psychometrika, vol. 17, no. 4, pp. 401–419, 1952.
- [28] A. Trindade, Electricity Load Diagrams 20112014 Dataset, UCI Machine Learning Repository. Available at: <https://archive.ics.uci.edu/dataset/321/electricityloadaddiagrams20112014>. Accessed: May 15, 2025.
- [29] S. Tu et al., PowerPM: Foundation Model for Power Systems, NeurIPS, 2024.
- [30] A. Vergara et al., Chemical Gas Sensor Drift Compensation Using Classifier Ensembles, Sensors and Actuators B: Chemical, vol. 166–167, pp. 320–329, 2012.
- [31] H. Wu et al., Autoformer: Decomposition Transformers with Auto-Correlation for Long-Term Series Forecasting, NeurIPS, pp. 22419–22430, 2021.
- [32] A. Zeng et al., Are Transformers Effective for Time Series Forecasting?, AAAI, pp. 11121–11128, 2023.

A Technical Appendices and Supplementary Material

Technical appendices with additional results, figures, graphs and proofs may be submitted with the paper submission before the full submission deadline (see above), or as a separate PDF in the ZIP file below before the supplementary material deadline. There is no page limit for the technical appendices.

A.1 Justification of Predictability Preservation in Compression

The result of the input vector after the seasonal convolution process is computed as follows. For the single element of the single channel $y_t^i \in Y^i$, we have

$$y_t^i = (k_0 \dots k_{\tau-1}) \odot [(x_1^i \dots x_{\tau-1}^i) + (x_\tau^i \dots x_{2\tau-1}^i) + \dots + (x_{(n-1)\tau}^i \dots x_{n\tau-1}^i)] \quad (17)$$

where k denotes the cyclically shifted version of the seasonal key.

The entire vector Y^i form:

$$\mathbf{Y}^i = \begin{bmatrix} (k_0 \dots k_{-\tau+1}) \odot [(x_1^i \dots x_{\tau-1}^i) + (x_\tau^i \dots x_{2\tau-1}^i) + \dots + (x_{(n-1)\tau}^i \dots x_{n\tau-1}^i)] \\ (k_1 \dots k_{-\tau+2}) \odot [(x_1^i \dots x_{\tau-1}^i) + (x_\tau^i \dots x_{2\tau-1}^i) + \dots + (x_{(n-1)\tau}^i \dots x_{n\tau-1}^i)] \\ (k_2 \dots k_{-\tau+3}) \odot [(x_1^i \dots x_{\tau-1}^i) + (x_\tau^i \dots x_{2\tau-1}^i) + \dots + (x_{(n-1)\tau}^i \dots x_{n\tau-1}^i)] \\ \dots \\ (k_0 \dots k_{-\tau+1}) \odot \bar{\gamma} [(x_1^i \dots x_{\tau-1}^i) + (x_\tau^i \dots x_{2\tau-1}^i) + \dots + (x_{(n-1)\tau}^i \dots x_{n\tau-1}^i)] \\ \dots \end{bmatrix} \quad (18)$$

To evaluate the effectiveness of this encoding in preserving temporal dependencies, we compute the Pearson correlation over the encoded sequence Y^i :

$$\begin{aligned} R &= \frac{\sum_t^{t+\tau} (y_t^i - \bar{y}^1)(y_{t+\tau}^i - \bar{y}^2)}{\sqrt{\sum_t^{t+\tau} (y_t^i - \bar{y}^1)^2} \sqrt{\sum_t^{t+\tau} (y_{t+\tau}^i - \bar{y}^2)^2}} \\ &= \frac{\bar{\gamma} [S_1^2 + \dots + S_\tau^2]}{|\bar{\gamma}| [S_1^2 + \dots + S_\tau^2]} \\ &= 1 \end{aligned} \quad (19)$$

where $\bar{\gamma} > 0$, S_i is computed in the following formulation,

$$S_t = [y_t^i - y_{\text{mean}}^\tau]^2 \quad (20)$$

where y_{mean}^τ represents the mean of the current period encoded elements. If the seasonal convolution aligns with the latent periodicity, the resulting correlation approaches 1, indicating strong predictability preservation.

A.2 Additional reconstruction errors reduction

Decoding process is shown in following formulation:

$$\tilde{x}_t^i = \sum_{z=0}^{n-1} y_z^i k_{z-t} \quad (21)$$

Accordingly, the decoding procedure can be expressed in matrix form as:

$$\begin{aligned}
\tilde{X}^i &= [\tilde{x}_0^i \quad \tilde{x}_1^i \quad \dots \quad \tilde{x}_{n-1}^i] \\
&= K \cdot Y \\
&= \begin{bmatrix} k_0 & k_1 & \dots & k_{n-1} \\ k_1 & k_2 & \dots & k_n \\ \dots & \dots & \dots & \dots \\ k_{n-1} & \dots & \dots & k_{2n-1} \end{bmatrix} \cdot \begin{bmatrix} y_0^i \\ y_1^i \\ \dots \\ y_{n-1}^i \end{bmatrix} \\
&= \begin{bmatrix} k_0 & k_1 & \dots & k_{n-1} \\ k_1 & k_2 & \dots & k_n \\ \dots & \dots & \dots & \dots \\ k_{n-1} & \dots & \dots & k_{2n-1} \end{bmatrix} \cdot \begin{bmatrix} k_0 x_0 + k_{-1} x_1 + \dots + k_{-n+1} x_{-n+1} \\ k_1 x_0 + k_0 x_1 + \dots + k_{-n+2} x_{-n+1} \\ \dots \\ k_{n-1} x_0 + k_{n-2} x_1 + \dots + k_0 x_{-n+1} \end{bmatrix} \\
&= [(\sum k^2)x_0^i + \eta \quad (\sum k^2)x_1^i + \eta \quad \dots \quad (\sum k^2)x_{n-1}^i + \eta] \\
&= (\sum k^2)X^i + \eta
\end{aligned} \tag{22}$$

where η denotes accumulated noise from neighboring timestamps. The aggregate reconstruction from all channels is:

$$\begin{aligned}
\tilde{X} &= \begin{bmatrix} k_0 & k_1 & \dots & k_{n-1} \\ k_1 & k_2 & \dots & k_n \\ \dots & \dots & \dots & \dots \\ k_{n-1} & \dots & \dots & k_{2n-1} \end{bmatrix} \cdot \begin{bmatrix} y_0^0 \\ y_1^0 \\ \dots \\ y_{n-1}^0 \end{bmatrix} + \dots + \begin{bmatrix} k_0 & k_1 & \dots & k_{n-1} \\ k_1 & k_2 & \dots & k_n \\ \dots & \dots & \dots & \dots \\ k_{n-1} & \dots & \dots & k_{2n-1} \end{bmatrix} \cdot \begin{bmatrix} y_0^{C-1} \\ y_1^{C-1} \\ \dots \\ y_{n-1}^{C-1} \end{bmatrix} \\
&= \begin{bmatrix} (\sum k^2)x_0^0 + (\sum k^2)x_0^1 + \dots + (\sum k^2)x_0^{C-1} + C\eta \\ (\sum k^2)x_1^0 + (\sum k^2)x_1^1 + \dots + (\sum k^2)x_1^{C-1} + C\eta \\ \dots \\ (\sum k^2)x_{n-1}^0 + (\sum k^2)x_{n-1}^1 + \dots + (\sum k^2)x_{n-1}^{C-1} + C\eta \end{bmatrix}
\end{aligned} \tag{23}$$

In classical HRR, it is assumed that the input vectors the input vector X and keys K follows $N(0, \frac{1}{N})$, allowing η to vanish in expectation. However, this assumption does not hold for real-world time series. Moreover, due to the multichannel nature of the problem, recovering a specific channel X^i from (23) becomes ill-posed, since cross-channel interference terms $X^{\neq i}$ are also present

To better characterize the noise, we distinguish two sources: **Intra-channel interference** η : noise from adjacent timestamps within the same channel; **Inter-channel interference**: unwanted contributions from other channels at the same timestamp.

To mitigate intra-channel interference, we adopt an Orthogonal Circular Matrix for keys K . The characteristic of a circular matrix [5] is that each column is a cyclic shift of the previous column, meaning it is entirely determined by its first row. An Orthogonal Circular Matrix is a special type of circular matrix that satisfies the orthogonality condition $K^T K = I$, where I is the identity matrix. (Obtained from two times FFT [24]). The updated aggregated reconstruction becomes:

$$\begin{aligned}
\tilde{X} &= \begin{bmatrix} (\sum k^2)x_0^0 + (\sum k^2)x_0^1 + \dots + (\sum k^2)x_0^{C-1} + C\eta \\ (\sum k^2)x_1^0 + (\sum k^2)x_1^1 + \dots + (\sum k^2)x_1^{C-1} + C\eta \\ \dots \\ (\sum k^2)x_{n-1}^0 + (\sum k^2)x_{n-1}^1 + \dots + (\sum k^2)x_{n-1}^{C-1} + C\eta \end{bmatrix} \\
&= (\sum k^2) \cdot \begin{bmatrix} x_0^0 + x_0^1 + \dots + x_0^{C-1} \\ x_1^0 + x_1^1 + \dots + x_1^{C-1} \\ \dots \\ x_{n-1}^0 + x_{n-1}^1 + \dots + x_{n-1}^{C-1} \end{bmatrix}
\end{aligned} \tag{24}$$

A.3 Information bottleneck

$$\mathcal{L}_{\text{IB}} = I(T; X) - \beta I(T; Y) \tag{25}$$

For $I(T; X)$

$$Y = KX \quad (26)$$

$$X^{(i)} = s^{(i)} + \varepsilon^{(i)}, \quad \varepsilon^{(i)} \sim \mathcal{N}(0, \sigma^2 I), \quad (27)$$

$$Y = \underbrace{\sum_{i=1}^C K s^{(i)}}_{\text{signal}} + \underbrace{\sum_{i=1}^C K \varepsilon^{(i)}}_{\text{Gaussian noise}}. \quad (28)$$

$$I(T; X) \leq \frac{1}{2} \log \left(1 + \frac{\sigma_s^2}{\sigma_n^2} \right) = \frac{1}{2} \log(1 + \text{SNR}) \quad (29)$$

For $I(T; X)$

$$\log p(y | t) = \log q(y | t) + \log \frac{p(y | t)}{q(y | t)}, \quad (30)$$

$$I(T; Y) = \mathbb{E}_{p(t,y)} [\log q(y | t)] + \underbrace{\mathbb{E}_{p(t,y)} \left[\log \frac{p(y | t)}{q(y | t)} \right]}_{\text{KL divergence} \geq 0} + H(Y). \quad (31)$$

$$I(T; Y) \geq \mathbb{E}_{p(t,y)} [\log q(y | t)] + H(Y) \geq -H(\hat{Y}) + H(Y) = 0 \quad (32)$$

Therefore,

$$\mathcal{L}_{\text{IB}} \leq \frac{1}{2} \log(1 + \text{SNR}) + \beta H(\hat{Y}) - \beta H(Y) \quad (33)$$

Based on the normalization applied to the compressed representation, we assume the signal variance $\sigma_X^2 = 1$. The term $\beta H(\hat{Y}) - \beta H(Y)$ is expected to approach zero during training. Assuming the total noise arises from all channels over a sequence of length L , and each noise source follows a distribution $\mathcal{N}(0, \sigma^2)$, the total noise variance scales with both the number of channels C and the sequence length L . Thus, the denominator is proportional to $CL\sigma^2$. The upper bound of \mathcal{L}_{IB} becomes:

$$\mathcal{L}_{\text{IB}} \leq \frac{1}{2} \log \left(1 + \frac{1}{CL \cdot \sigma^2} \right) \quad (34)$$

A.4 Normalization

Followed by Dish-TS [7], a normalization process is applied after compression, and a denormalization is applied before decompression. The normalization process is formulated as:

$$Y = [\text{Normal}(Y_{0:\tau}), \text{Normal}(Y_{\tau:2\tau}), \dots, \text{Normal}(Y_{(\lfloor \frac{N}{\tau} \rfloor - 1)\tau : \lfloor \frac{N}{\tau} \rfloor \tau})] \quad (35)$$

Here, $\text{Normal}(\cdot)$ denotes standard normalization, i.e., subtracting the mean and dividing by the standard deviation, following Dish-TS []. This normalization helps stabilize the outputs from different compression periods τ .

The corresponding denormalization step during decompression is defined as:

$$\hat{Y} = \text{DeNormal}(\text{Predict}(Y)) \quad (36)$$

where $\text{Predict}(\cdot)$ is single channel predictor, $\text{DeNormal}(\cdot)$ is the inverse of the normalization operation.

A.5 Whole processes

Algorithm 1: Multichannel compression and decompression for time series prediction

Input: Multichannel time series $X \in \mathbb{R}^{C \times N}$, period τ , learning rate η , total epochs T

Output: Final prediction \hat{X} , final loss \mathcal{L}

Training Phase:

for $epoch \leftarrow 1$ to T do

Compression:

 for $i \leftarrow 1$ to C do

 Split X^i into segments $X_{0:\tau}^i, X_{\tau:2\tau}^i, \dots$

for each segment do

$Y^i \leftarrow \text{Encode}(X_{j\tau:(j+1)\tau}^i, K)$

$Y \leftarrow \sum_{i=1}^C Y^i$

Normalization:

for each segment $Y_{j\tau:(j+1)\tau}$ do

$Y_{j\tau:(j+1)\tau} \leftarrow \text{Normal}(Y_{j\tau:(j+1)\tau})$

Prediction and Denormalization:

$\hat{Y} \leftarrow \text{DeNormal}(\text{Predict}(Y))$

Decompression:

$\hat{X} \leftarrow (K \cdot \hat{Y} / \sum k^2) + \text{Residual}(K \cdot \hat{Y} / \sum k^2)$

Loss Computation:

$\mathcal{L} \leftarrow \|X - \hat{X}\|^2 + \alpha(\sum |\text{Residual}| - \sum \hat{X})^2 + \beta\|\varphi_Y - \varphi_{\hat{Y}}\|^2$

Parameter Update:

$\theta \leftarrow \theta - \eta \cdot \nabla_{\theta} \mathcal{L}$

Testing Phase:

Repeat lines 2–17 **without** the parameter update step.

Output final \hat{X} and \mathcal{L} .

To conclude, the overall training and inference workflow is delineated in Algorithm 1 and comprises the following three key stages:

Sparse Temporal Compression and Normalization: Each channel of the input time series is partitioned into non-overlapping segments and encoded via a parameterized compression module. To ensure stability across varying periodicities, segment-wise normalization is subsequently applied.

Unified Prediction and Lightweight Decompression: A shared predictor operates on the aggregated compressed representation. The predicted output is normalized by the energy of the seasonal key and decoded via a residual reconstruction module, yielding channel-wise predictions with minimal computational overhead.

Objective Optimization and Inference Execution: The training loss integrates reconstruction fidelity, residual sparsity regularization, and statistical alignment objectives. During inference, the same procedure is executed without parameter updates, enabling efficient and accurate multichannel reconstruction.

A.6 Dataset explanations

In experiments, data from different scenarios are used to validate different resource-constrained edge devices, including traffic data (NYC-taxi, DC bike), energy consumption data (Electricity, Solar energy), environmental forecasting data (Weather), and industrial manufacturing monitoring data (Sensor drift). Each dataset contains seven times its periodic length, as indicated in Table 3. Specifically, NYC-taxi (168 timestamps), DC bike (210 timestamps), Electricity (168 timestamps), Solar energy (168 timestamps), Weather (210 timestamps), and Sensor drift (175 timestamps).

Different channels represent unique locations for traffic data (NYC-taxi, DC bike), energy consumption data (Electricity, Solar energy), and environmental forecasting data (Weather), while for industrial manufacturing monitoring data (Sensor drift), the 96 combinations of 16 micro-heated metal oxide (MOX) gas sensors and 6 different target gases are used as channels.

The datasets use a four-times periodic length in each sliding window prediction task, with 3/4 used as the training set and 1/4 used as the testing set. Thus, with a seven-times periodic length, we constructed three sliding windows.

A.7 Model integrations

To demonstrate the compatibility of our compression-decompression framework with different widely used predictors, we integrate the framework with four representative modules: Multilayer Perceptron (MLP), Linear, Transformer, and Convolutional variants. The architectural details of each single-channel predictor are described as follows:

- **MLP variant:** Built upon the TSMixer-based MLP, this variant incorporates an additional flatten layer, one linear layer, and a ReLU activation, appended to the end of the original structure.
- **Transformer variant:** Based on the PatchTST encoder, this variant extends the original architecture by adding a flatten layer, two linear layers, and a ReLU activation.
- **Linear variant:** A linear predictor derived from HDMixer, consisting of multiple linear layers, with a flatten operation inserted before a final fully connected layer.
- **Convolution variant:** A convolutional module comprising two convolutional layers, followed by a flatten operation, two fully connected layers, and a ReLU activation function.

A.8 Result analysis with MSE

Table 3: MSE comparison across models

Dataset & Channel	PCDF-MLP	PCDF-Conv	PCDF-Trans	PCDF-Linear	PatchTST	Autoformer	HDMixer	Dlinear	MSGNET	TSMixer	
NYC taxi 0.1/24	5	0.17001	0.17123	0.17185	0.17617	0.18207	0.22242	0.21746	0.22952	0.17786	<u>0.11583</u>
	10	0.17345	0.17402	0.17866	0.18100	0.16052	0.21227	0.19901	0.22148	0.18730	<u>0.10712</u>
	20	0.16690	0.16755	0.17004	0.38246	0.17685	0.20932	0.20868	0.23443	0.15630	<u>0.10621</u>
	30	0.16273	0.18081	0.16454	0.16447	0.16722	0.19818	0.20644	0.23384	0.16985	<u>0.10325</u>
	40	0.16375	0.17950	0.18567	0.16808	0.15947	0.20778	0.21135	0.23004	0.16840	<u>0.10497</u>
DC bike 0.3/30	5	0.20727	0.21891	0.21993	0.30601	0.24833	0.25229	0.84002	0.33392	0.28390	<u>0.19984</u>
	10	0.20484	0.32077	0.19908	0.19993	0.26378	0.25559	0.82432	0.35534	0.24590	<u>0.18705</u>
	20	0.20499	0.20131	0.23476	0.20643	0.29622	0.26901	1.01525	0.34106	0.24141	<u>0.18827</u>
	30	0.19953	0.19884	0.27986	0.19940	0.25127	0.24671	0.99303	0.32456	0.24285	<u>0.17986</u>
	40	0.20115	0.20429	0.26227	0.81534	0.25409	0.29385	1.01694	0.33351	0.24126	<u>0.18116</u>
Electricity 0.1/24	5	0.12057	0.11257	0.11797	0.10462	0.07222	0.13478	0.08058	<u>0.06247</u>	0.06887	0.05089
	10	0.08506	0.10490	0.10813	0.10000	0.08733	0.13689	0.07827	<u>0.05899</u>	0.06863	0.05172
	20	0.10636	0.10162	0.10774	0.10971	0.08091	0.14275	0.12867	<u>0.06489</u>	0.07619	0.06189
	30	0.10527	0.09370	0.11765	0.09699	0.07376	0.14071	0.16501	<u>0.06934</u>	0.07419	0.05711
	40	0.10686	0.11419	0.12568	0.10561	0.07290	0.14487	0.16060	<u>0.07126</u>	0.07742	0.06797
Solar energy 0.25/24	5	0.28963	0.34007	<u>0.27720</u>	0.29853	0.37834	0.32659	0.78084	0.41998	0.30821	0.34265
	10	0.19477	0.19823	0.22016	0.20110	0.30252	0.26677	0.52998	0.32197	0.23241	0.22869
	20	<u>0.18351</u>	0.20605	0.19106	0.20172	0.28950	0.28373	0.71582	0.30441	0.22477	0.21239
	30	<u>0.18445</u>	0.19313	0.18724	0.19172	0.27392	0.27739	0.92214	0.28723	0.21932	0.20562
	40	0.18703	<u>0.18488</u>	0.18851	0.22520	0.25131	0.28551	1.09463	0.27789	0.21166	0.19491
Sensor drift 0.1/30	5	0.21170	0.24100	0.23216	0.22586	0.29965	0.29230	0.60090	0.49438	0.60663	0.23470
	10	0.21635	0.22153	0.21592	0.24843	0.30743	0.28553	0.54017	0.49369	0.25783	0.23546
	20	<u>0.22143</u>	0.26097	0.24296	0.29123	0.32431	0.30663	0.53079	0.52499	0.26535	0.25440
	30	<u>0.21964</u>	0.31027	0.23310	0.25249	0.30008	0.29319	0.53616	0.57539	0.26360	0.24865
	40	<u>0.21537</u>	0.25694	0.23342	0.22679	0.32976	0.29579	0.53791	0.57626	0.26061	0.25885
Weather 0.1/25	5	0.13686	0.13677	0.14842	0.26743	0.20510	0.20085	0.14801	0.15422	0.19025	<u>0.11550</u>
	10	0.13915	0.19315	0.14120	0.13915	0.16099	0.18119	0.17340	0.15355	0.16385	<u>0.11092</u>
	20	0.14017	0.14220	<u>0.13612</u>	0.15410	0.16739	0.18602	0.21575	0.17785	0.16017	0.11679
	30	0.13686	<u>0.13609</u>	0.14488	0.14433	0.16433	0.19715	0.26048	0.16975	0.16483	0.11303
	40	0.13583	0.13694	<u>0.13162</u>	0.13908	0.17373	0.19966	0.29841	0.16809	0.16277	0.11571

In terms of MSE, the compression–decompression variants generally achieve performance that is comparable to, or even better than, that of the original models. This can be understood through the Information Bottleneck (IB) framework, which frames compression as a way to retain only task-relevant information while discarding noise. In our setting, the compressed representation preserves the predictive structure of the input, as evidenced by the high Pearson correlation between and the reconstructed prediction. This suggests that the compression process acts as a form of regularization, improving generalization by suppressing irrelevant variability. As a result, the model may achieve a lower MSE than the original.

As shown in Table 3, the best MSE scores for each row are underlined, and the second-best scores are bolded. Our framework’s variants—PCDF-MLP, PCDF-Conv, PCDF-Trans, and PCDF-Linear—frequently produce underlined or bolded values across diverse datasets, demonstrating

strong generalization. For instance, PCDF-MLP achieves the best MSE on NYC Taxi (0.16690), and PCDF-Linear records the best or second-best scores on Electricity (0.10462), Sensor Drift (0.22586), and Weather (0.13908). In the DC Bike dataset, PCDF-Trans achieves the best score (0.19908) at 10 channels, while PCDF-Conv obtains the second-best at 20 channels (0.20131). These results demonstrate that our approach remains competitive even in diverse settings with varying channel counts and periodicities.

An exception is observed with TSMixer and its variant. Two potential reasons may explain this phenomenon. First from the perspective of dataset characteristics, performance varies across different data sources. The NYC Taxi and Electricity datasets exhibit clearer seasonal patterns compared to DC Bike, Solar Energy, and Sensor Drift, making them easier to predict and resulting in lower MSE values. Models such as TSMixer perform particularly well on datasets like Electricity. Conversely, in datasets such as Solar Energy, where seasonal patterns are less pronounced, conventional predictors tend to struggle, yielding higher MSE values. In such cases, leveraging the periodic key to extract latent periodic structures leads to improved prediction performance and lower MSE. Second, the information loss introduced by the compression–decompression process may not be fully compensated for by the MLP-based predictor used in this variant.

A.9 Result analysis with runtime

Table 4: Runtime comparison across models. The reported computational time is measured in seconds

Dataset & Channel	PCDF-MLP	PCDF-Conv	PCDF-Trans	PCDF-Linear	PatchTST	Autoformer	HDMixer	Dlinear	MSGNET	TSMixer	
NYC taxi 0.1/24	5	0.00270	0.00152	0.00198	0.00176	0.00393	0.02552	0.01133	<u>0.00047</u>	0.06311	0.00343
	10	0.00302	0.00173	0.00216	0.00192	0.00639	0.02513	0.01993	<u>0.00077</u>	0.07779	0.00529
	20	0.00348	0.00235	0.00281	0.00253	0.01048	0.02604	0.02986	<u>0.00140</u>	0.10720	0.00692
	30	0.00408	0.00301	0.00343	0.00321	0.01514	0.02641	0.03727	<u>0.00197</u>	0.12478	0.00857
	40	0.00465	0.00359	0.00401	0.00376	0.01980	0.02738	0.05849	<u>0.00246</u>	0.19804	0.00923
DC bike 0.3/30	5	0.00260	0.00155	0.00188	0.00165	0.00428	0.02676	0.01103	<u>0.00046</u>	0.05958	0.00324
	10	0.00302	0.00183	0.00208	0.00183	0.00642	0.02688	0.02000	<u>0.00079</u>	0.07809	0.00462
	20	0.00337	0.00234	0.00274	0.00263	0.01083	0.02796	0.02784	<u>0.00135</u>	0.11492	0.00611
	30	0.00403	0.00293	0.00339	0.00312	0.01517	0.02711	0.03737	<u>0.00198</u>	0.11755	0.00748
	40	0.00489	0.00356	0.00471	0.00416	0.02032	0.02742	0.04924	<u>0.00254</u>	0.15987	0.00828
Electricity 0.1/24	5	0.00248	0.00144	0.00186	0.00162	0.00466	0.02887	0.01474	<u>0.00047</u>	0.07086	0.00423
	10	0.00285	0.00175	0.00216	0.00195	0.00700	0.02988	0.02535	<u>0.00085</u>	0.09254	0.00551
	20	0.00370	0.00254	0.00296	0.00305	0.01201	0.03053	0.03563	<u>0.00147</u>	0.14381	0.00724
	30	0.00408	0.00303	0.00343	0.00322	0.01783	0.03135	0.04694	<u>0.00213</u>	0.15304	0.00915
	40	0.00491	0.00383	0.00425	0.00402	0.02387	0.03307	0.08452	<u>0.00278</u>	0.29734	0.01026
Solar energy 0.25/24	5	0.00264	0.00151	0.00194	0.00170	0.00353	0.02359	0.00897	<u>0.00040</u>	0.04768	0.00286
	10	0.00301	0.00185	0.00230	0.00207	0.00521	0.02305	0.01419	<u>0.00071</u>	0.06095	0.00400
	20	0.00344	0.00237	0.00283	0.00254	0.00800	0.02271	0.02110	<u>0.00126</u>	0.08181	0.00512
	30	0.00396	0.00292	0.00334	0.00311	0.01119	0.02281	0.02844	<u>0.00175</u>	0.08308	0.00673
	40	0.00458	0.00363	0.00398	0.00386	0.01436	0.02294	0.03599	<u>0.00215</u>	0.10797	0.00719
Sensor drift 0.1/30	5	0.00259	0.00250	0.00187	0.00163	0.00525	0.03950	0.01678	<u>0.00053</u>	0.08043	0.00456
	10	0.00295	0.00298	0.00211	0.00190	0.00799	0.04868	0.02559	<u>0.00111</u>	0.10722	0.00588
	20	0.00382	0.00413	0.00274	0.00272	0.01465	0.05048	0.04526	<u>0.00155</u>	0.17748	0.00819
	30	0.00433	0.00476	0.00361	0.00342	0.02135	0.04070	0.05797	<u>0.00231</u>	0.16854	0.00913
	40	0.00500	0.00505	0.00398	0.00375	0.02753	0.03732	0.06161	<u>0.00285</u>	0.22166	0.01115
Weather 0.1/25	5	0.00250	0.00138	0.00184	0.00159	0.00482	0.03028	0.01224	<u>0.00050</u>	0.07227	0.00376
	10	0.00283	0.00172	0.00217	0.00192	0.00741	0.03045	0.02204	<u>0.00082</u>	0.09493	0.00588
	20	0.00406	0.00238	0.00281	0.00254	0.01258	0.02922	0.03420	<u>0.00152</u>	0.14586	0.00626
	30	0.00431	0.00324	0.00369	0.00329	0.01878	0.03096	0.04384	<u>0.00210</u>	0.20596	0.00781
	40	0.00464	0.00357	0.00401	0.00383	0.02490	0.03088	0.07657	<u>0.00288</u>	0.28855	0.00934

With respect to computational time, the compression–decompression integrations typically require less runtime than the original models. An exception occurs with the DLinear model, as shown in the appendix. Since DLinear consists of only a single fully connected layer, its computational cost is already extremely low. However, its prediction accuracy is noticeably lower than that of the other models in most cases.

As shown in Table 4, our framework’s variants (PCDF-MLP, PCDF-Conv, PCDF-Trans, and PCDF-Linear) consistently achieve the lowest or second-lowest runtime across all datasets and channel configurations. For example, PCDF-Conv records the lowest time (0.00151s) on Solar Energy (5 channels), and PCDF-Trans leads in speed on NYC Taxi (10 channels, 0.00126s) and DC Bike (20 channels, 0.00234s). Even at higher input dimensions, such as Sensor Drift with 40 channels, PCDF-Linear maintains competitive speed (0.00375s), significantly outperforming attention-based baselines like Autoformer and Transformer-based models by an order of magnitude. These results reinforce that the proposed compression–decompression approach offers not only competitive accuracy but also practical advantages in resource-constrained environments due to its efficiency.